energies

MDPI

Article

Numerical Study on the Effects of Water and Heat Transport on Two-Phase Flow in a Polymer Electrolyte Membrane Fuel Cell

Dapeng Gong [1], Sichuan Xu [1], Xuhui Wang [2] and Yuan Gao [1,*]

[1] School of Automotive Studies, Tongji University, Shanghai 200092, China
[2] China Automotive Engineering Research Institute Co., Ltd., Chongqing 401122, China
* Correspondence: rays_chien@hotmail.com

Abstract: A one-dimensional transient non-isothermal model was developed to study the two-phase flow phenomenon in a polymer electrolyte membrane fuel cell. The model focused on the phase change between vapor and liquid water, and the transport of oxygen, hydrogen, water, and heat. The cell was discretized into 39 control volumes, and the finite volume method and the iteration method were used to solve the transport equations. The variations in the state parameters of the model during fuel cell operations were analyzed. The results showed that, when the inlet gas humidity was high, the vapor tended to condense in gas diffusion layer regions close to the gas channel. As temperatures in these regions were low, the vapor was more likely to condense. Liquid water appeared latest in the middle of the anode gas diffusion layer, because the vapor concentration in this area is always lower than its saturated value. A higher operating temperature in a cell is beneficial to prevent flooding at the cathode.

Keywords: polymer electrolyte membrane fuel cell; two-phase flow; heat transport; phase change; one-dimensional model; finite volume method

Citation: Gong, D.; Xu, S.; Wang, X.; Gao, Y. Numerical Study on the Effects of Water and Heat Transport on Two-Phase Flow in a Polymer Electrolyte Membrane Fuel Cell. *Energies* **2022**, *15*, 8318. https://doi.org/10.3390/en15218318

Academic Editor: Antonino S. Aricò

Received: 13 October 2022
Accepted: 2 November 2022
Published: 7 November 2022

1. Introduction

Polymer electrolyte membrane fuel cells (PEMFCs) are promising power devices to replace conventional internal-combustion machines because of their high efficiency, high energy density, and zero emissions. The essence of PEMFCs is an electrochemical reaction generator, which can convert chemical energy into electrical energy through the reverse process of water electrolysis [1]. As shown in Figure 1, the gas from the cathode and anode flow channels diffuses through the porous gas diffusion layer to the catalyst layer. Under the catalysis of platinum inside the anode catalyst layer, the hydrogen molecule decomposes into protons and electrons during the hydrogen oxidation reaction. The protons are then transferred to the cathode catalyst layer through the proton-exchange membrane (PEM), whereas the electrons travel through an external circuit. Water is mainly generated via the oxygen reduction reaction in the cathode catalyst layer [2]. It diffuses through the PEM and migrates between the anode and cathode under the forces of electro-osmotic drag, concentration permeation, and hydraulic permeation [3–5]. The overall electrochemical reaction inside a fuel cell is accompanied by energy generation. Ion transportation produces electricity, which can provide power for an external load, i.e., the vehicle.

Proper management of water and heat transport in a PEMFC system is essential to improve its overall performance and durability [6]. In a PEM, the ionic conductivity is determined by the water content. A high water content will greatly improve the membrane's proton conductivity, consequently decreasing the membrane's ohmic resistance and increasing the fuel cell's output voltage [7]. An external humidifier is usually adopted to humidify the cathode inlet gas to keep the membrane moist. When the water production rate in the CL is higher than its removal rate, accumulated liquid water will submerge pores in the gas diffusion layer (GDL) and CL, leading to a flooding phenomenon and blocking passages for reaction gas transport [8]. The key point of water management is to maintain

the water content in the membrane at a proper value and remove the liquid water generated from electrochemical reactions out of cells in time. Flooding is typically observed at the cathode side, as water production mainly occurs at the cathode. However, water is more likely to back-diffuse from the cathode to the anode as the PEM becomes thinner [9]. When hydrogen recirculation is adopted in a hydrogen supply system, back-diffused water from the cathode will also be recirculated and accumulated at the anode, resulting in possible anode water flooding [10–12]. Therefore, it is necessary to study the mechanisms of water transport, water phase change, and liquid water capillary transport in both the GDL and CL. If the partial pressure of water vapor is higher than the saturated value, the water vapor will condense into liquid water. When the vapor temperature is below the freezing point, icing problems will be major concerns during PEMFC cold-start operations. Many studies on PEMFCs focused on the internal water phase change [13–15]. The two-phase flow of water vapor and liquid water is another important issue. Liquid water transport in porous structures relies on capillary forces and is affected by the porosity, hydrophilicity and hydrophobicity, and surface tension of the material [4,16]. A hydrophobic surface is beneficial for water drainage, while a high content of polytetrafluoroethylene is helpful to form a hydrophobic surface [17–19]. Several researchers managed to establish capillary transport functions based on their experiments, and some of those functions have been widely used in numerical studies [20,21].

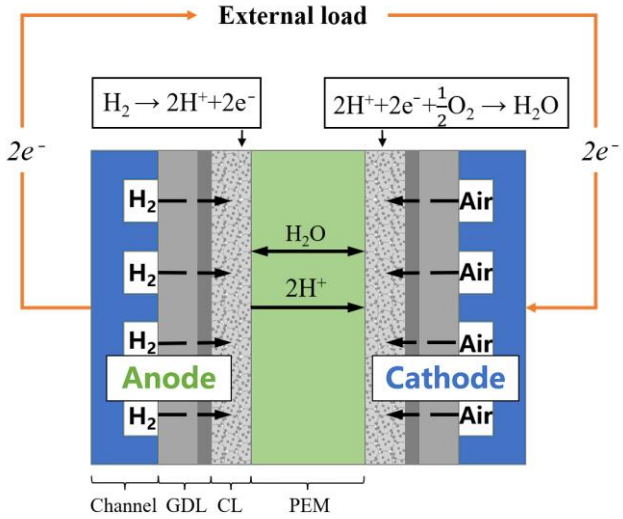

Figure 1. Schematic of a single PEMFC.

Several numerical models were proposed to investigate the mechanisms of water and heat transport and two-phase flow in PEMFCs. Wang et al. [20,22–24] compared a single-phase flow model with a two-phase model and found that the two-phase model was more accurate in predicting the PEMFC's performance. They also investigated the differences between the unsaturated flow theory and the multi-phase mixture model and concluded that the multi-phase mixture model was more convenient when solving two-phase co-existing zones. Lei et al. [25] proposed a two-dimensional, steady-state, non-isothermal model to study the mechanisms of water phase change and thermal transport. Their results showed that a high operation temperature can accelerate the electrochemical reaction, reduce liquid water saturation, and hence improve the PEMFC's performance.

Two-dimensional and three-dimensional models can characterize PEMFC's internal chemical and physical processes more precisely, but require high computational power and complex modeling procedures. Instead, one-dimensional models need less computational power and are more suitable for building dynamic PEMFC models and transient simulations. Haddad et al. [26] developed a one-dimensional model to investigate the distributions of water and electrical charges in a cell. Hu et al. [27] studied the transient

phenomena of two-phase transport in GDL and proposed a procedure to identify the phase change based on a one-dimensional isothermal model.

In this research, a one-dimensional transient non-isothermal model was developed to analyze the effects of water and heat transport on two-phase flow. Gas transport, liquid water capillary transport, dissolved water transport, heat transport, and phase change between water vapor and liquid water were considered in the model. Variations in the heat and water distribution in a cell were investigated under a loading–unloading operation. The effects of heat transport on the concentration of saturated vapor and the distribution of water vapor were also studied [28].

2. Model Development

2.1. Model Assumptions

A one-dimensional model was built to investigate the water transport and temperature distribution in a single cell. As illustrated in Figure 2 [29], the model comprised a PEM layer sandwiched between layers of endplates, coolant channels, gas channels, GDLs, and CLs at both the cathode and anode. The anode gas channel (AGC), cathode gas channels (CGCs), anode catalyst layer (ACL), cathode catalyst layer (CCL), and PEM were all equally divided into three parts, while the anode gas diffusion layer (AGDL) and cathode gas diffusion layer (CGDL) were composed of ten uniform segments, respectively. The anode end-plate (AEP), anode coolant channel (ACC), cathode end-plate (CEP), and cathode coolant channel (CCC) were all considered as homogeneous lumped models. Several assumptions were made, as follows:

1. Water is initially generated in the CCL. When the water content in the PEM is higher than the equilibrium value, the dissolved water turns into water vapor;
2. Water vapor condenses when its partial pressure is higher than the saturated vapor pressure, while liquid water evaporates when the vapor partial pressure is below the saturated value;
3. In gas channels, only convection in the Y direction and diffusion in the X direction are considered;
4. Gases cannot penetrate the PEM.

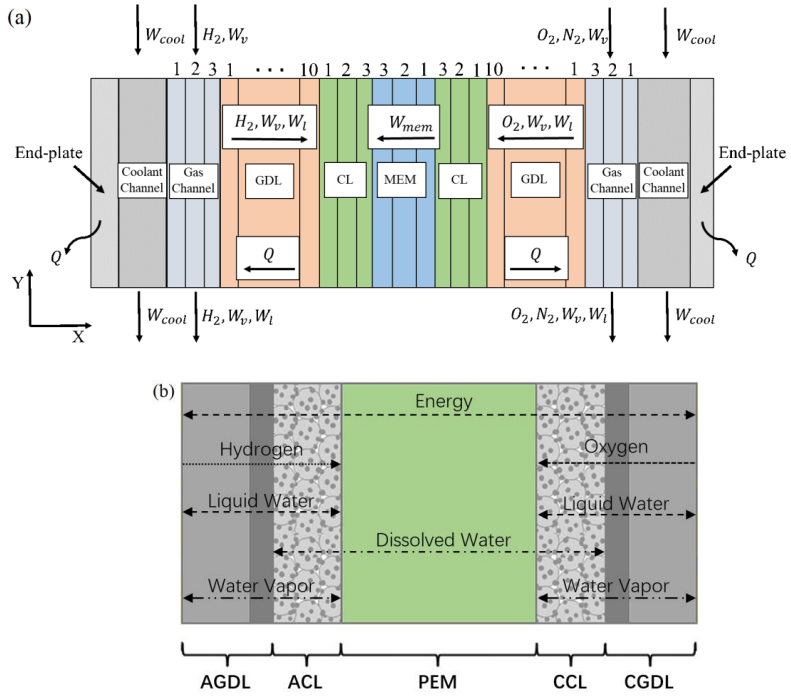

Figure 2. Schematic of (**a**) the PEMFC one-dimensional model and (**b**) computational domain with major heat and mass transfer processes.

2.2. Gas Diffusion in GDL and CL

Hydrogen, oxygen, and water vapor accomplish transportation through diffusion in the GDL and CL in this model. Gas diffusion mainly depends on its concentration gradient and travels from a high-concentration region to a low-concentration region. Oxygen and water vapor diffuse in the CGDL and CCL, and hydrogen and water vapor diffuse in the AGDL and ACL. The volume of pores and liquid water existing in the GDL and CL are both considered, as they have significant effects on diffusion. The gas transport equation is expressed in Equation (1)

$$\frac{\varepsilon(1-s)\,\partial C_i}{\partial t} = \nabla\left(D_i^{eff}\nabla C_i\right) + S_i \tag{1}$$

In Equation (1), the left term denotes the accumulation rate of gas species i, and the first term on the right side is the diffusion flux. ε is the porosity of the CL or GDL, s is the liquid saturation, which is a volume ratio of liquid water to pores, C_i and S_i express the mole concentration and source term of the gas species i, respectively, and D^{eff} is the effective diffusion coefficient of a gas in the CL and GDL. C_i is calculated as

$$C_i = \frac{P_i}{RT} \tag{2}$$

where P_i is the partial pressure of species i, R is the gas constant, and T is the temperature.

The diffusion coefficient in the CL and GDL depends on their porosity, tortuosity, and liquid water fraction, which needs to be corrected according to the Bruggeman correlation. The Knudsen diffusion coefficient (D_i^{nu}) should be taken into account, as the mean radius of pores in the CL is around 0.1 µm [30,31]. The effective diffusivity D_i^{eff} and Knudsen diffusivity D_i^{nu} are expressed as Equations (3)–(5)

$$D_i^{eff} = D_i^k \varepsilon^{1.5}(1-s)^{1.5} \tag{3}$$

$$D_i^{nu} = \frac{2}{3}\sqrt{\frac{8RT}{\pi M_i}} \tag{4}$$

$$D_i^k = \begin{cases} D_i & (\text{in GDL}) \\ \left(\frac{1}{D_i} + \frac{1}{D_i^{nu}}\right)^{-1} & (\text{in CL}) \end{cases} \tag{5}$$

where D_i and M_i denote the diffusion coefficient of species i and molecular weight, respectively.

Oxygen and hydrogen are consumed in the CCL and ACL, respectively. It is assumed that the consumption rate in each region of the CL is the same. The phase change is considered in the water vapor transport. The source item S_i for species i and phase change rate between vapor and liquid water are defined in Table 1.

Table 1. Source terms in transport equations.

No.	Source Term	Unit
1	$S_{O_2} = \begin{cases} \frac{j}{4F} & (\text{in CCL}) \\ 0 & (\text{in other zones}) \end{cases}$	mol m^{-3} s^{-1}
2	$S_{H_2} = \begin{cases} \frac{j}{2F} & (\text{in ACL}) \\ 0 & (\text{in other zones}) \end{cases}$	mol m^{-3} s^{-1}
3	$S_v = \begin{cases} S_{dv}M_w - S_{vl} & (\text{in CL}) \\ -S_{vl}\,M_w & (\text{in GDL}) \end{cases}$	mol m^{-3} s^{-1}

Table 1. *Cont.*

No.	Source Term	Unit
4	$S_{vl} = \begin{cases} \gamma_{con}\varepsilon(1-s)\dfrac{P_v - P_{sat}}{RT} & P_v \geq P_{sat} \\ \gamma_{eva}\varepsilon s\dfrac{P_v - P_{sat}}{RT} & P_v < P_{sat} \end{cases}$	mol m^{-3} s^{-1}
5	$S_{mem} = \begin{cases} \dfrac{j}{2F} - S_{dv} (\text{in CCL}) \\ -S_{dv} \ \ (\text{in ACL}) \end{cases}$	mol m^{-3} s^{-1}
6	$S_{dv} = \xi\dfrac{\rho_{mem}}{EW}(\lambda_{di} - \lambda_{eq})(1-s)$	mol m^{-3} s^{-1}
7	$S_{gc} = \begin{cases} S_{vl} & for\ water\ vapor \\ 0 & for\ O_2\ or\ H_2 \end{cases}$	mol m^{-3} s^{-1}
8	$Q = \begin{cases} j\left(\eta_{act} + \dfrac{T\Delta S}{4F}\right) + j\eta_{om} + h_{con}(S_{vl} - S_{dv}) & (\text{in cathode CL}) \\ j\eta_{om} + h_{con}(S_{vl} - S_{dv}) & (\text{in anode CL}) \\ j\eta_{om} & (\text{in membrane}) \\ h_{con}S_{vl} & (\text{in GDL}) \\ -h_{end\_env}(T_{end} - T_{env}) & (\text{in end} - \text{plate}) \\ -m_{cool}C_p^w\left(T_{cool} - T_w^{in}\right) & (\text{in coolant channel}) \\ -m_g C_p^g\left(T_{ch} - T_g^{in}\right) + h_{con}S_{vl} & (\text{in gas channel}) \end{cases}$	W m^{-3} s^{-1}

2.3. Liquid Water Capillary Transport in GDL and CL

In the CL and GDL, the capillary pressure gradient drives the liquid water migration, which can be described by Equation (6)

$$\frac{\varepsilon\rho_{lq}\partial s}{\partial t} = \nabla\left(\rho_{lq}D_{lq}\nabla s\right) + S_{vl}M_w \tag{6}$$

where ρ_{lq} and D_{lq} are the density and diffusion coefficient of liquid water in the CL or GDL, respectively.

The viscosity of liquid water (μ_{lq}) and capillary pressure (P_c) determine the diffusion coefficient, and the relation can be described as

$$D_{lq} = -\frac{K_0K_r}{\mu_{lq}}\frac{dP_c}{ds} \tag{7}$$

where K_0 is the liquid phase permeability and K_r is the relative permeability of liquid water ($K_r = s^4$).

The capillary pressure was dramatically influenced by the physical and geometric parameters of the GDL and CL. The contact angle (θ) is usually used to distinguish whether a surface is hydrophobic or hydrophilic. When the contact angle is less than 90°, the surface is hydrophilic, and vice versa. The capillary pressure is expressed by Equation (8):

$$p_c = \begin{cases} \sigma\cos\theta\left(\frac{\varepsilon}{K_0}\right)^{0.5}\left(1.417(1-s) - 2.12(1-s)^2 + 1.263(1-s)^3\right) & \theta < 90^\circ \\ \sigma\cos\theta\left(\frac{\varepsilon}{K_0}\right)^{0.5}\left(1.417s - 2.12s^2 + 1.263s^3\right) & \theta > 90^\circ \end{cases} \tag{8}$$

where σ is the surface tension of liquid water.

2.4. Dissolved Water Transport in PEM and CL

Three main methods were taken into consideration to solve the water transportation in the PEM, i.e., the electro-osmotic drag, concentration permeation, and hydraulic permeation, among which the concentration permeation, or the concentration diffusion, is affected by the concentration gradient of the dissolved water. The hydraulic permeation is

so small that it is commonly neglected in model developments compared with the other two methods [2]. The transport equation of the dissolved water is shown in Equation (9).

$$\frac{\rho_{mem}}{EW}\frac{\partial(\omega\lambda_{di})}{\partial t} = \nabla\left(\frac{\rho_{mem}}{EW}\omega^2 D_{dmw}\nabla\lambda_{di}\right) + \nabla\left(\frac{2.5\lambda_{di}i}{22F}\right) + S_{mem} \quad (9)$$

The left side of the equation calculates the accumulation rate of the dissolved water, the first term on the right side denotes the concentration diffusion transport, the second term represents the electro-osmotic drag, and the last term S_{mem} is the source term. ρ_{mem} is the density of the PEM in dry state, EW is the equivalent weight of the PEM, ω is the volume fraction of the ionomer in the CL, λ_{di} is the water content in the ionomer, which is related to the PEM density and water concentration ($\lambda_{di} = \frac{EW}{\rho_{mem}C_{H2O}}$), D_{dmw} is the diffusion coefficient of dissolved water, and i is the current density. The value of D_{dmw} in this study is solved by using the correlations in Equation (10) suggested by Motupally et al. [32].

$$D_{dmw} = \begin{cases} 3.1\times10^{-7}\lambda_{di}[\exp(0.28\lambda_{di})-1]\exp\left(-\frac{2346}{T}\right) & \lambda_{di} < 3 \\ 4.17\times10^{-8}\lambda_{di}[161\exp(0.28\lambda_{di})+1]\exp\left(-\frac{2346}{T}\right) & 3 \le \lambda_{di} < 17 \end{cases} \quad (10)$$

In the CCL, the water source term contains water generated from both the electrochemical reaction and phase change from vapor to dissolved water. In the ACL, there is only the phase-changed water. The source term, S_{mem}, is expressed in Table 1.

The equilibrium water content is a function of the water activity (a) and temperature. Two correlations of the equilibrium water content at 80 and 30 °C proposed by Zawodzinski et al. [33] and Spinger et al. [34] were applied. Linear interpolation was adopted to determine the equilibrium water content between the two temperatures. The above correlations are described in Equations (11)–(13).

$$\lambda_{eq}|_{30°C} = \begin{cases} 0.043 + 17.81a - 39.85a^2 + 36a^3 & a \le 1 \\ 14.0 + 1.4(a-1) & a > 1 \end{cases} \quad (11)$$

$$\lambda_{eq}|_{80°C} = \begin{cases} 1.409 + 11.26a - 18.77a^2 + 16.21a^3 & a \le 1 \\ 10.11 + 2.944(a-1) & a > 1 \end{cases} \quad (12)$$

$$\lambda_{eq} = \left(\lambda_{eq}|_{80°C} - \lambda_{eq}|_{30°C}\right)\left(\frac{T-303}{353-303}\right) + \lambda_{eq}|_{30°C} \quad (13)$$

The water activity is related to both the liquid saturation and relative humidity, calculated as

$$a = \frac{C_v}{C_{sat}} + 2s \quad (14)$$

2.5. Two-Phase Transport in Gas Channels

Liquid water existing in gas channels originates from the diffusion across the GDL, and is blown out by a large-flux gas flowing through the channel. The governing equations of gas and water transport can be expressed as Equations (15) and (16).

$$\frac{(1-s)\partial C_i}{\partial t} + \nabla(u_g C_i) = \nabla(D_i\cdot\nabla C_i) + S \quad (15)$$

$$\frac{\rho_{lq}\partial s}{\partial t} + \nabla\left(\rho_{lq}u_{lq}s\right) = \nabla\left(D_{lq\_ch}\cdot\nabla s\right) + S_{vl}M_w \quad (16)$$

where u_g and u_{lq} are the flow rates of gas and liquid water, respectively, and their relationship is defined as

$$u_{lq} = Xu_g \quad (17)$$

where X is the flow rate ratio of liquid to gas.

Pressure loss in the channel is related to the gas dynamic viscosity, channel geometry, and gas flow rate, which can be calculated using Equation (18) [35,36]

$$\Delta P = \frac{16L}{3ZA_{ch}d_{ch}^2}[V_{in}(2\mu_{in} + \mu_{out}) + V_{out}(\mu_{in} + 2\mu_{out})] \tag{18}$$

where L and d_{ch} are the length and hydraulic diameter of the channel, respectively, Z is the number of channels, A_{ch} is the cross-section area of the channel, and V_{in} and V_{out} are the volume flow rates of the inlet and outlet gases, respectively.

According to the ideal gas law, the gas volume flow rate is expressed using Equation (19)

$$V = \frac{RT\sum_i N_i}{P} \tag{19}$$

where N_i is the molar flow rate of species i.

The dynamic viscosity of a gas mixture is described in Equation (20)

$$\mu = \sum_i x_i \mu_i \tag{20}$$

where x_i is the molar fraction of gas species i.

The gas velocity in the channel is simplified as the mean value of the inlet and outlet gas velocities, and is calculated with Equations (21)–(23).

$$u_{in} = \frac{V_{in}RT}{P_{in}ZA_{ch}} \tag{21}$$

$$u_{out} = \frac{V_{out}RT}{P_{out}ZA_{ch}} \tag{22}$$

$$u_g = \frac{(u_{in} + u_{out})}{2} \tag{23}$$

where P_{out} is the difference between the inlet pressure and pressure loss in the channel, as described in Equation (24).

$$P_{out} = P_{in} - \Delta P \tag{24}$$

2.6. Energy Conservation

For energy conservation in this model, thermal diffusion is the primary term, while the thermal convection term is neglected. The energy conservation equation is shown in Equation (25) specifically.

$$\frac{\partial((\rho C_p)_{eff}T)}{\partial t} = \nabla\cdot\left(k_{eff}\nabla T\right) + Q \tag{25}$$

where $(\rho C_p)_{eff}$ is the effective volumetric heat capacity on the left side, and k_{eff} is the effective thermal conductivity on the right side.

In view of the differences between the physical parameters of gas, liquid water, and carbon, evaluating the effects of liquid water, reactant gases, and pores on heat transport is necessary. The effective thermal conductivity and effective volumetric heat capacity are calculated as Equations (34) and (35)

$$(\rho C_p)_{eff} = \begin{cases} \varepsilon s(\rho C_p)_{lq} + \varepsilon(1-s)(\rho C_p)_g + (1-\varepsilon-\omega)(\rho C_p)_c + \omega(\rho C_p)_{mem} & (\text{inCL}) \\ \varepsilon s(\rho C_p)_{lq} + \varepsilon(1-s)(\rho C_p)_g + (1-\varepsilon)(\rho C_p)_c & (\text{inCDL}) \\ (\rho C_p)_{mem} & (\text{inmembrane}) \\ (\rho C_p)_{ch} & (\text{ingaschannelandcoolantchannel}) \\ (\rho C_p)_{end} & (\text{inend}-\text{plate}) \end{cases} \tag{26}$$

$$k_{eff} = \begin{cases} \varepsilon s k_l + \varepsilon(1-s)k_g + (1-\varepsilon-\omega)k_c + \omega k_{mem} & (\text{inCL}) \\ \varepsilon s k_l + \varepsilon(1-s)k_g + (1-\varepsilon)k_c & (\text{inCDL}) \\ k_{mem} & (\text{inmembrane}) \\ k_{ch} & (\text{ingaschannelandcoolantchannel}) \\ k_{end} & (\text{end}-\text{plate}) \end{cases} \quad (27)$$

The volumetric heat capacity of the reactant gas is calculated by Equation (28).

$$(\rho C_p)_g = \sum_i x_i (\rho C_p)_i \quad (28)$$

Heat generation in the model comes from the voltage overpotential, ohmic resistance, electrochemical reaction, and latent heat of phase change. It is dissipated primarily by cooling water in coolant channels, reactant gases in gas channels, and endplates. Definitions of the relative source terms are provided in Table 1.

2.7. Cell Voltage

The three main losses in cell potentials are activation overvoltage, ohmic overvoltage, and concentration overvoltage, and the output voltage (U_{out}) is defined as

$$U_{out} = E_{nerst} - \eta_{act} - \eta_{oh} - \eta_{mt} \quad (29)$$

where E_{nerst} is the thermodynamic potential and η_{act}, η_{oh}, and η_{mt} are the activation overvoltage, ohmic overvoltage, and concentration overvoltage, respectively. According to the Nernst equation, E_{nerst} can be calculated using Equation (30).

$$E_{nerst} = 1.23 - 0.9 \times 10^{-3}(T - 298) + \frac{RT_0}{2F}\left(lnP_{H_2}^{in} + \frac{1}{2}lnP_{O_2}^{in}\right) \quad (30)$$

The activation overvoltage is calculated using the Butler–Volmer equation given below, which is mainly determined by the electrochemical reaction rate.

$$\eta_{act} = \frac{RT}{4\alpha F}\ln\left(\frac{j}{(1-s)j_{ca}^{ref}\frac{C_{O_2}^{CL}}{C_{O_2}^{ref}}}\right) \quad (31)$$

where α is the transfer coefficient, j_{ca}^{ref} is the reference current density, and $C_{O_2}^{ref}$ is the reference oxygen concentration.

The ohmic overvoltage is determined as

$$\eta_{oh} = i \cdot A_{cell} \cdot R_\Omega \quad (32)$$

where R_Ω is the overall resistance. R_Ω can be calculated using Equations (33)–(35).

$$R_\Omega = \frac{\delta_{mem}}{\kappa_{ion}^{eff}} + \frac{\delta_{CL}}{2\kappa_{ion}^{eff}} + \frac{\delta_{CL}}{2\kappa_{ele}^{eff}} + R_{contact} \quad (33)$$

$$\kappa_{ion}^{eff} = \omega^{1.5}\kappa_{ion} \quad (34)$$

$$\kappa_{ele}^{eff} = (1-\varepsilon-\omega)^{1.5}\kappa_{ele} \quad (35)$$

In these equations, δ and κ are the thickness and ionic conductivity of the CL or PEM, respectively.

The ionic conductivity of the ionomer is determined by the internal water content and temperature, which can be calculated as:

$$\kappa_{ion} = \left(0.5139\lambda_{nf} - 0.326\right)\exp\left[1268\left(\frac{1}{303.15} - \frac{1}{T}\right)\right] \quad (36)$$

The differences in oxygen concentration between the CL and channels result in concentration overvoltage. η_{mt} can be described by Equation (37).

$$\eta_{mt} = \frac{RT}{\alpha F} \ln\left(\frac{C_{O_2}^{cl}}{C_{O_2}^{ch}}\right) \tag{37}$$

3. Boundary Conditions

3.1. Inlet Boundaries

The concentrations of oxygen and water vapor and the fraction of liquid water at the inlet of the CGC are given in Equations (38)–(40)

$$C_{O_2}^{in}|_{\mathrm{CGC}} = 0.21\frac{\left(P_{ca}^{in} - RH_{ca}^{in}P_{sat}\right)}{RT_g^{in}} \tag{38}$$

$$C_v^{in}|_{\mathrm{CGC}} = \frac{RH_{ca}^{in}P_{sat}}{RT_g^{in}} \tag{39}$$

$$s_{in}|_{\mathrm{CGC}} = 0 \tag{40}$$

where RH is the relative humidity.

The molar flow rates at the inlet of the CGC, are described by Equations (41)–(43)

$$N_{O_2}^{in}|_{\mathrm{CGC}} = \psi_{ca}\frac{i}{4F}A_{cell} \tag{41}$$

$$N_{N_2}^{in}|_{\mathrm{CGC}} = \frac{0.79}{0.21} \times N_{O_2}|_{\mathrm{CGC}} \tag{42}$$

$$N_v^{in}|_{\mathrm{CGC}} = \frac{x_v}{x_{O_2}}N_{O_2}^{in}|_{\mathrm{CGC}} \tag{43}$$

where ψ_{ca} is the stoichiometry ratio at the cathode.

Similarly, the concentrations and molar flow rates at the inlet of the AGC can be obtained from Equations (44)–(48).

$$C_{H_2}^{in}|_{\mathrm{AGC}} = \frac{\left(P_{an}^{in} - RH_{an}^{in}P_{sat}\right)}{RT_{an}^{in}} \tag{44}$$

$$C_v^{in}|_{\mathrm{AGC}} = \frac{RH_{an}^{in}P_{sat}}{RT_{an}^{in}} \tag{45}$$

$$s_{in}|_{\mathrm{AGC}} = 0 \tag{46}$$

$$N_{H_2}^{in}|_{\mathrm{AGC}} = \psi_{an}\frac{i}{2F}A_{cell} \tag{47}$$

$$N_v^{in}|_{\mathrm{AGC}} = \frac{x_v}{x_{H_2}}N_{H_2}^{in}|_{\mathrm{CGC}} \tag{48}$$

3.2. Outlet Boundaries

The outlets of gas channels are regarded as fully developed boundaries, which can be described by Equations (58) and (59).

$$\frac{\partial C_i}{\partial y} = 0 \tag{49}$$

$$\frac{\partial s}{\partial y} = 0 \tag{50}$$

3.3. Other Boundaries

Fully developed boundary conditions were applied to solve gas and liquid water transport equations at the interface between the CL and PEM, as well as the interface between the gas channels and coolant channels. The heat transport boundary between endplates and the environment is also considered to be fully developed. The boundaries are listed in Equations (51)–(55). The boundary at the interface between the GDL and CL is described by Equation (56).

$$\frac{\partial C_i}{\partial x}|_{\mathrm{CL}-mem} = 0 \tag{51}$$

$$\frac{\partial C_i}{\partial x}|_{\mathrm{GC}-\mathrm{CC}} = 0 \tag{52}$$

$$\frac{\partial s}{\partial x}|_{\mathrm{CL}-mem} = 0 \tag{53}$$

$$\frac{\partial s}{\partial x}|_{\mathrm{GC}-\mathrm{CC}} = 0 \tag{54}$$

$$\frac{\partial T}{\partial x}|_{\mathrm{EP}-envir} = 0 \tag{55}$$

$$\frac{\partial \lambda_{di}}{\partial x}|_{\mathrm{GDL}-\mathrm{CL}} = 0 \tag{56}$$

4. Numerical Procedures

Solving the above partial differential equations (PDE) is the key point of the model. The finite volume method was used to discretize these PDEs, and convergence of the calculation was achieved using the iteration method.

4.1. Finite Volume Method

The principle by which the finite volume method solves a one-dimensional model is shown in Figure 3, in which a computational domain is discretized into a number of control volumes, and each control volume is represented by its central node [37]. The transport equations in this model are nonstationary, which can be expressed as the general forms shown in Equation (57) [38]. If integrated in spatial scale and time scale, Equation (57) can be replaced with Equation (58).

$$\frac{\partial(\rho\phi)}{\partial t} + \frac{\partial}{\partial x}(\rho u\phi) = \frac{\partial}{\partial x}\left(D\frac{\partial\phi}{\partial x}\right) + S \tag{57}$$

$$\int_t^{t+\Delta t}\int_{\Delta V}\frac{\partial(\rho\phi)}{\partial t}dVdt + \int_t^{t+\Delta t}\int_{\Delta V}\frac{\partial}{\partial x}(\rho u\phi)dVdt = \int_t^{t+\Delta t}\int_{\Delta V}\frac{\partial}{\partial x}\left(D\frac{\partial\phi}{\partial x}\right)dVdt + \int_t^{t+\Delta t}\int_{\Delta V}SdVdt \tag{58}$$

where ΔV is the control volume ($\Delta V = A\Delta x$).

The calculation at node P in Figure 3 is described as Equation (59)

$$\rho\left(\phi_P - \phi_P^0\right)\Delta x + \int_t^{t+\Delta t}\left[(\rho u\phi)_e - (\rho u\phi)_w\right]dt = \int_t^{t+\Delta t}\left[\left(D\frac{\partial\phi}{\partial x}\right)_e - \left(D\frac{\partial\phi}{\partial x}\right)_w\right]dt + \int_t^{t+\Delta t}S\Delta x dt \tag{59}$$

where ϕ_P^0 is the value at the last time step.

After being discretized through a fully implicit method, Equation (59) transforms into Equation (60).

$$\rho\left(\phi_P - \phi_P^0\right)\frac{\Delta x}{\Delta t} + \rho u_e\frac{\phi_E + \phi_P}{2} - \rho u_w\frac{\phi_W + \phi_P}{2} = D_e\frac{\phi_E - \phi_P}{\delta x_{PE}} - D_w\frac{\phi_P - \phi_W}{\delta x_{PW}} + S\Delta x \tag{60}$$

Equation (60) can be expressed as Equations (61)–(65)

$$a_P\phi_P = a_W\phi_W + a_E\phi_E + a_P^0\phi_P^0 + S\Delta x \tag{61}$$

$$a_W = \frac{\rho u_w}{2} + \frac{D_w}{\Delta x} \tag{62}$$

$$a_E = \frac{D_e}{\Delta x} - \frac{\rho u_e}{2} \tag{63}$$

$$a_P^0 = \rho\frac{\Delta x}{\Delta t} \tag{64}$$

$$a_P = a_P^0 + \frac{\rho u_e}{2} - \frac{\rho u_w}{2} + \frac{D_w}{\Delta x} + \frac{D_e}{\Delta x} \tag{65}$$

where $\Delta x = \delta x_{PE} = \delta x_{PW}$.

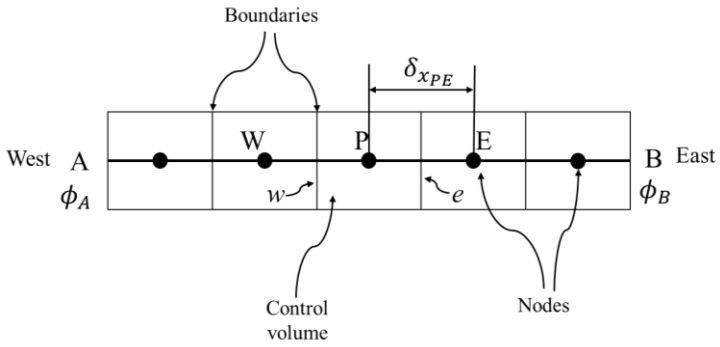

Figure 3. Schematic of the finite volume method for a one-dimensional model.

4.2. Model Validation

The calculation was conducted using MATLAB R2019a. The specific calculation procedure is described in Figure 4. In the calculation, the time step was set as 0.1 s. All variables were initialized at the beginning of each time step. Calculations were iterated until all residuals were below 10^{-8}. In the calculation of voltage, the effects of gas concentration, liquid water saturation, and water content on output voltage were considered.

The model was validated by comparing the numerical results with the experimental ones obtained by Sukkee et al. [39] and Yang et al. [40]. During the calculation, the parameters of the cell, i.e., the thicknesses of the GDL, CL, and PEM and porosities of the GDL and CL, were taken according to real values in physical cells used by Sukkee et al. and Yang et al. The results of the calculations and experiments are plotted in Figure 5a. As shown in Figure 5b, the simulation agreed well with Yang's experiments over the whole current density range. When the current density was 1.15 A/cm^2, the maximum relative error was 10.25%. Apart from this point, the relative error remained below 6%, and the average value was 3.31%. Regarding Sukkee's results, there was a good agreement between the calculated results and the measured data when the current density was within the range of 0 to 0.6 A/cm^2. The simulation slightly deviated from the experiment when the current density exceeded 0.6 A/cm^2, and the average relative error was 4.86%.

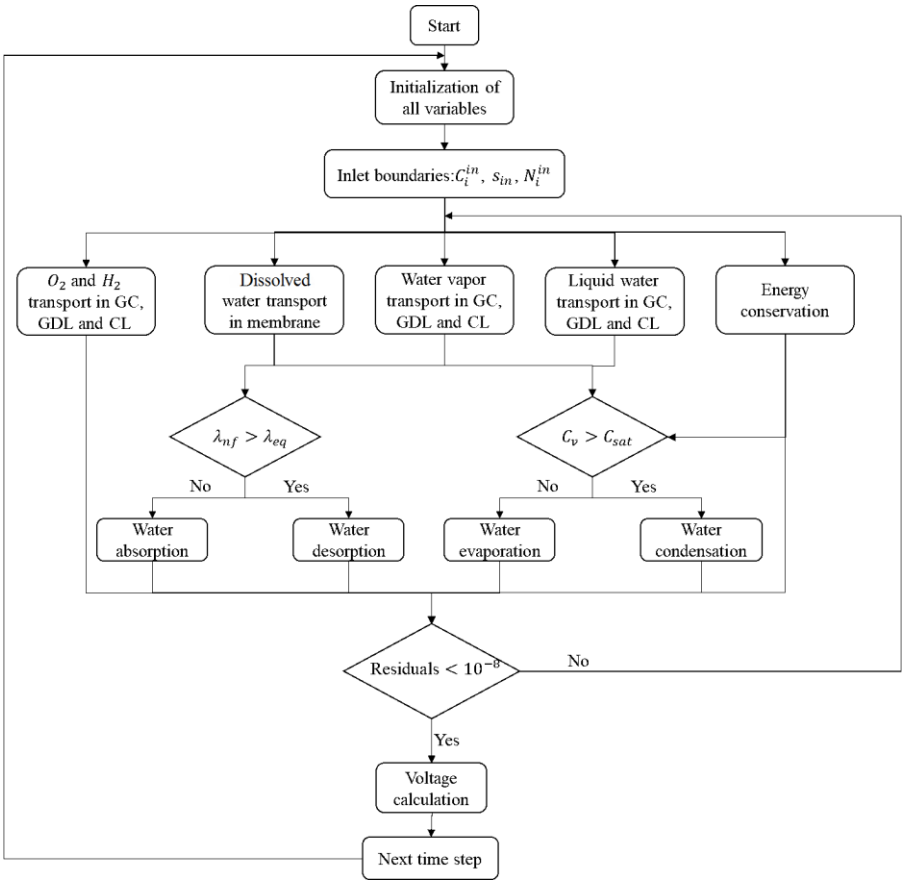

Figure 4. Schematic of the calculation procedure.

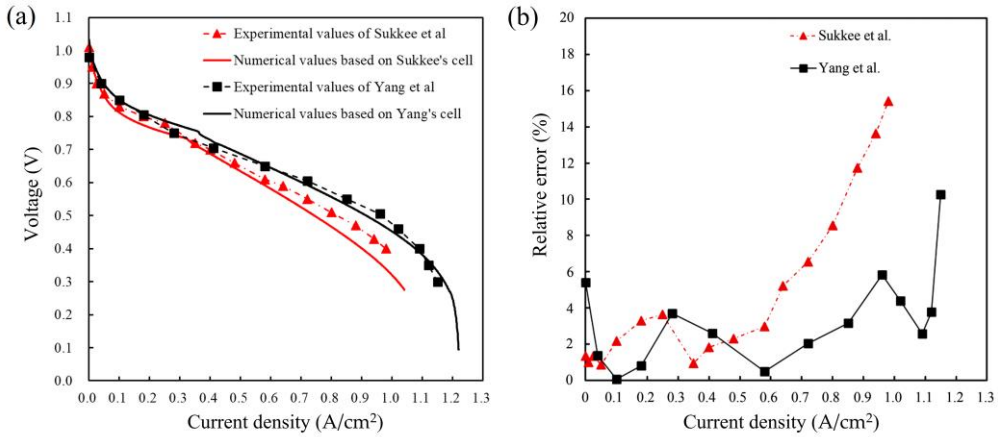

Figure 5. Model validation using experimental data obtained by Sukkee et al. [39] and Yang et al. [40]: (**a**) Polarization curves; (**b**) Relative error curves.

5. Results and Discussion

In this section, variations in water vapor, liquid water, temperature, and dissolved water are analyzed under a condition where the current density varies every 100 s. These terms in different regions illustrated in Figure 2 are expressed in a simple manner. For example, $T_{\mathrm{CL}}^{ca}(2)$ represents the temperature at the second region of the CL at the cathode, $C_{\mathrm{GDL}}^{an}(5)$ is the concentration at the fifth region of the GDL at the anode, and so on. Parameters, including the diffusion coefficient, dynamic viscosity, and phase change rate, are listed In Table 2. Geometric parameters of the cell and its material properties, such as the thicknesses of each layer, porosities of the GDL and CL, contact angles, etc., are listed in

Table 3. The initial and operating conditions, such as the relative humidity of inlet gases, stoichiometry, and temperatures, are provided in Table 4.

Table 2. Transport parameters.

Parameter	Correlation/Value	Unit
Oxygen diffusivity	$D_{O_2}^{ca} = 2.652 \times 10^{-5}\left(\frac{T}{333.15}\right)^{1.5}\left(\frac{101325}{P}\right)$	$m^2\ s^{-1}$
Water vapor diffusivity in the cathode	$D_v^{ca} = 2.982 \times 10^{-5}\left(\frac{T}{333.15}\right)^{1.5}\left(\frac{101325}{P}\right)$	$m^2\ s^{-1}$
Hydrogen and water vapor diffusivity in the anode	$D_v^{an} = D_{H_2}^{an} = 1.055 \times 10^{-4}\left(\frac{T}{333.15}\right)^{1.5}\left(\frac{101325}{P}\right)$	$m^2\ s^{-1}$
Oxygen dynamic viscosity	$\mu_{O_2} = 8.46 \times 10^{-3}\left(\frac{T}{292.25}\right)^{1.5}(T+127)^{-1}$	$kg\ m^{-1}\ s^{-1}$
Hydrogen dynamic viscosity	$\mu_{H_2} = 3.206 \times 10^{-3}\left(\frac{T}{293.85}\right)^{1.5}(T+72)^{-1}$	$kg\ m^{-1}\ s^{-1}$
Nitrogen dynamic viscosity	$\mu_{N_2} = 7.33 \times 10^{-3}\left(\frac{T}{300.55}\right)^{1.5}(T+111)^{-1}$	$kg\ m^{-1}\ s^{-1}$
Water vapor dynamic viscosity	$\mu_v = 7.512 \times 10^{-3}\left(\frac{T}{291.15}\right)^{1.5}(T+120)^{-1}$	$kg\ m^{-1}\ s^{-1}$
Evaporation rate	$\gamma_{eva} = 10^4$	s^{-1}
Condensation rate	$\gamma_{con} = 10^4$	s^{-1}
Water transfer rate	$\xi = 1.0$	s^{-1}
Latent heat of condensation	$h_{con} = -2438.5T + 3170700$	$J\ kg^{-1}$
Entropy change of reaction	$\Delta S = -326.36$	$J\ mol^{-1}\ K^{-1}$
Liquid to gas velocity ratio	0.05	
Transfer coefficient	$\alpha = 0.5$	
Reference current density	$j_{ca}^{ref} = 10^4 \exp\left[-7900\left(\frac{1}{T} - \frac{1}{353.15}\right)\right]$	$A\ m^{-3}$
Reference oxygen concentration	$C_{O_2}^{ref} = 40$	$mol\ m^{-3}$

Table 3. Material properties.

Parameter	Value	Unit
Thickness of the membrane (δ_{mem})	0.015	mm
Thickness of the CL (δ_{CL})	0.015	mm
Thickness of the GDL (δ_{mem})	0.30	mm
Thickness of the coolant channel (δ_{cc})	1.0	mm
Thickness of the end-plate (δ_{ep})	10.0	mm
Channel length (L_{ch})	20.0	mm
Channel width (d_{ch})	1.0	mm
Number of gas channels (Z)	10	
Cell area (A_{cell})	0.04	m^2
Porosity of the CL (ε_{CL})	0.25	

Table 3. *Cont.*

Parameter	Value	Unit
Porosity of the GDL ($\varepsilon_{\mathrm{GDL}}$)	0.6	
Volume fraction of the ionomer in the CL (ω)	0.2	
Contact angle of the CL (θ_{CL})	85	°
Contact angle of the GDL (θ_{GDL})	110	°
Intrinsic permeability of the CL (K_{CL})	6.2×10^{-13}	m^2
Intrinsic permeability of the GDL (K_{GDL})	6.2×10^{-12}	m^2
Equivalent weight of the membrane (EW)	1.1	g mol^{-1}
Dry density of the membrane (ρ_{mem})	1980	kg m^{-3}
Density of the CL (ρ_{CL}) and GDL (ρ_{GDL})	1000 and 1000	kg m^{-3}
Thermal conductivities of the membrane (k_{mem})	0.96	Wm^{-1} K^{-1}
Thermal conductivities of the GDL and CL (k_{GDL} *and* k_{CL})	1	Wm^{-1} K^{-1}
Thermal conductivity of the end-plate (k_{ep})	52	Wm^{-1} K^{-1}
Thermal conductivity of the channel (k_{ch})	52	Wm^{-1} K^{-1}
Specific heat capacity of the membrane $(C_p)_{mem}$	833	J kg^{-1} K^{-1}
Specific heat capacity of the GDL and CL $(C_p)_{\mathrm{GDL}}$ and $(C_p)_{\mathrm{CL}}$	710 and 710	J kg^{-1} K^{-1}
Specific heat capacity of the channel $(C_p)_{ch}$	935	J kg^{-1} K^{-1}

Table 4. Initial and operating conditions.

Parameter	Value	Unit
Initial temperature of the cell (T_0)	298	K
Environment temperature (T_{air})	298	K
Initial water content in the ionomer (λ_0)	4	
Relative humidity of inlet gas in the cathode (RH_{ca})	90%	
Relative humidity of inlet gas in the anode (RH_{an})	90%	
Stoichiometry in the cathode (ψ_{ca})	2	
Stoichiometry in the anode (ψ_{ca})	1.3	
Pressure of the inlet gases (P_{ca}^{in}, P_{an}^{in})	2	bar
Temperature of the inlet gases (T_{gas}^{in})	298	K
Temperature of the inlet coolant water (T_{cool}^{in})	333	K
Volume flow rate of the coolant water (V_{cool}^{in})	0.30	L min^{-1}

During the simulation, the current density was regulated to increase from 0.1 A/cm^2 at 0 s to 1.2 A/cm^2 at 400 s and then decrease to 0.8 A/cm^2 at 500 s and 0.3 A/cm^2 at 600 s. The corresponding output voltage during this process is presented in Figure 6. In the first 100 s, the initial ionic conductivity was low due to the low initial water content in PEM, leading to high ohmic loss and low initial voltage. With the membrane being humidified by the inlet gas with high humidity, the output voltage quickly recovered from 0.79 V at 0 s to 0.89 V at around 60 s. After the first 100 s, the output voltage was able to reach its stability shortly after the current changed and showed a converse trend with the current variation.

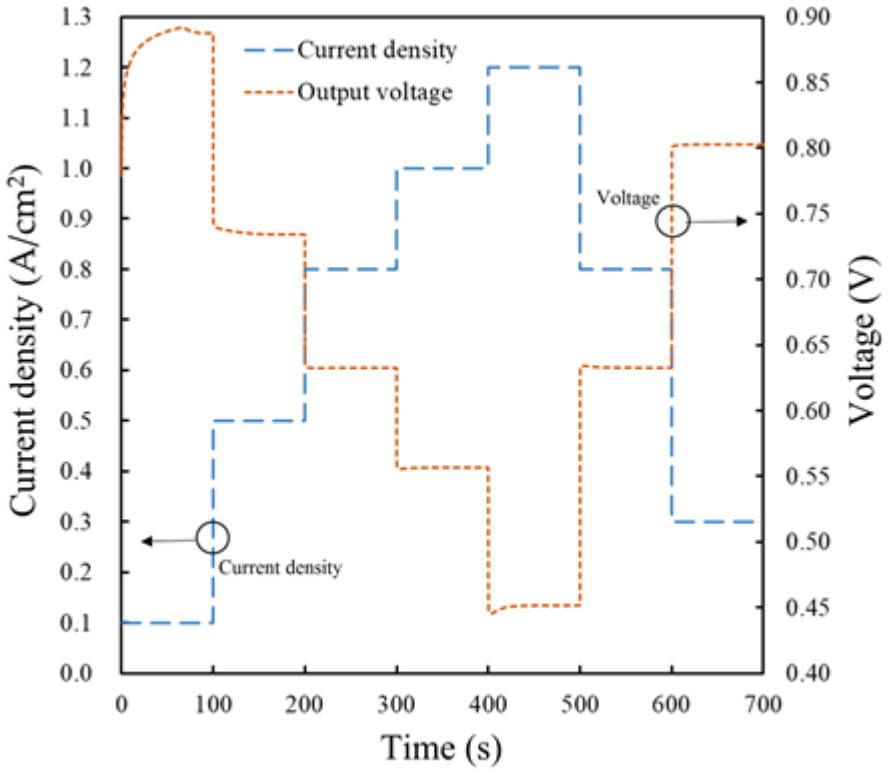

Figure 6. Variations in the output voltage and current density.

5.1. Temperature Distribution

As a PEMFC generally operates within a temperature range of 60 to 80 °C, the temperature of the inlet cooling water was set to 60 °C. The temperatures in each subarea of the cell varied during the running process, and some temperature distribution patterns in typical subareas are plotted in Figure 7a. In the initial 30 s, the cell's temperature increased quickly and the temperature difference between the regions was small. The quick increase in temperature during the initial moment was attributed to the warm coolant water. When the amount of heat produced was equal to the amount dissipated, the cell reached a steady working state, so the temperatures of each region remained stable. At this moment, heat was transferred from the CCL to the CEP and AEP. The heat generation rate was positively correlated with the current density. As the current density increased every 100 s, the temperature at each steady state increased and reached a new steady state accordingly. Correspondingly, the temperature decreased when the current density decreased after 500 s.

Figure 7b shows the distributions of the cell temperatures at 5 s and 150 s. At 5 s, the temperature of the coolant channel was higher than that of its neighbor regions. The heat generated from the oxygen reduction reaction was larger than that due to the hydrogen oxidation reaction, which caused the temperature at the cathode to be higher than that at the anode. At 150 s, the highest temperature appeared in the CCL, and the temperature in the CEP was slightly higher than that in the AEP, as indicated by the yellow line in Figure 7b.

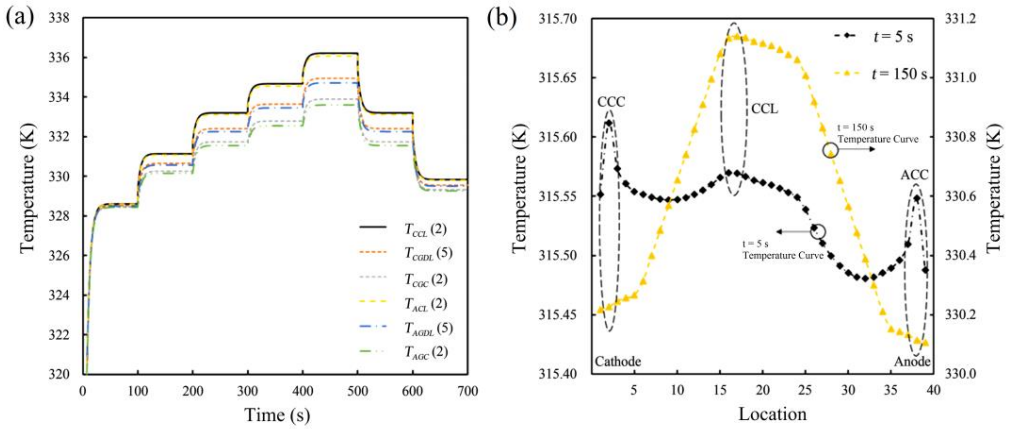

Figure 7. Variation in temperature during operation: (**a**) temperatures in the CL, GDL, and gas channels, and (**b**) distributions of temperature from the CEP to AEP at 5 s and 150 s.

5.2. Distributions of Water Vapor and Liquid Water on the Cathode Side

The distributions of and variations in liquid water and vapor in the cathode are shown in Figure 8. The patterns of the vapor concentrations in the CCL, CGDL, and CGC during the operation are shown in Figure 8a. It is clear that the membrane was humidified by the high-humidity inlet gas at the very beginning within 0 to 30 s, leading to only minor differences in the vapor concentrations at the cathode. When the vapor concentration in the CL was higher than that in the gas channel, the vapor in the CL began to move toward the gas channel. The highest vapor concentration depended on the saturation vapor pressure, which was mainly decided by the temperature. Hence, the water vapor concentration changed in a similar manner to the temperature, as shown in Figure 7a. Once the cell was loaded, the vapor concentration in the gas channel slightly declined because the mass flow rate of the inlet gas increased and the accumulated vapor was removed by the high-flux gas.

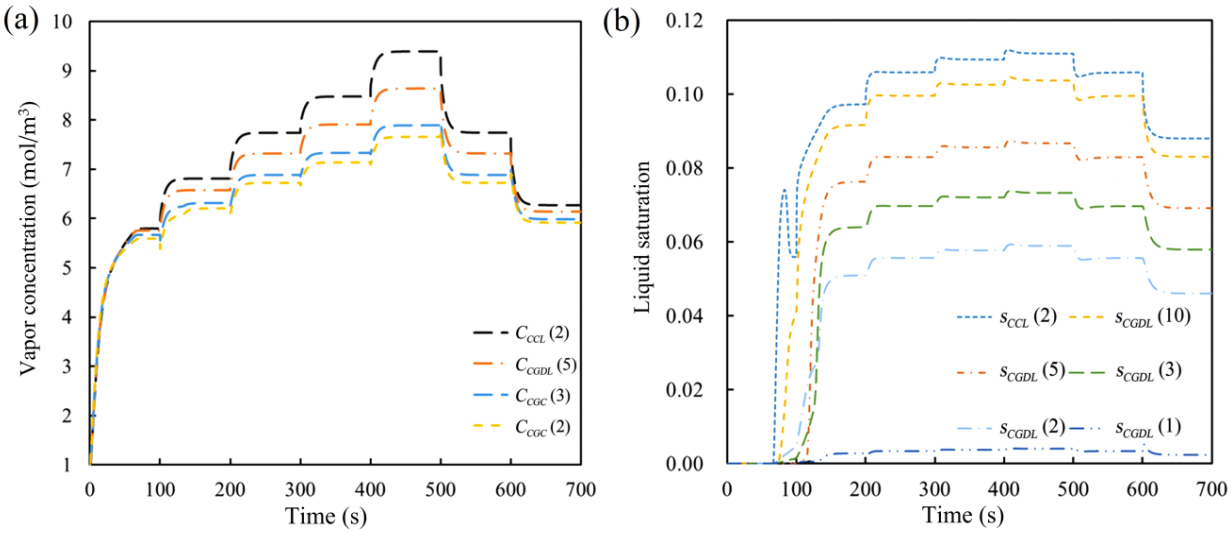

Figure 8. *Cont.*

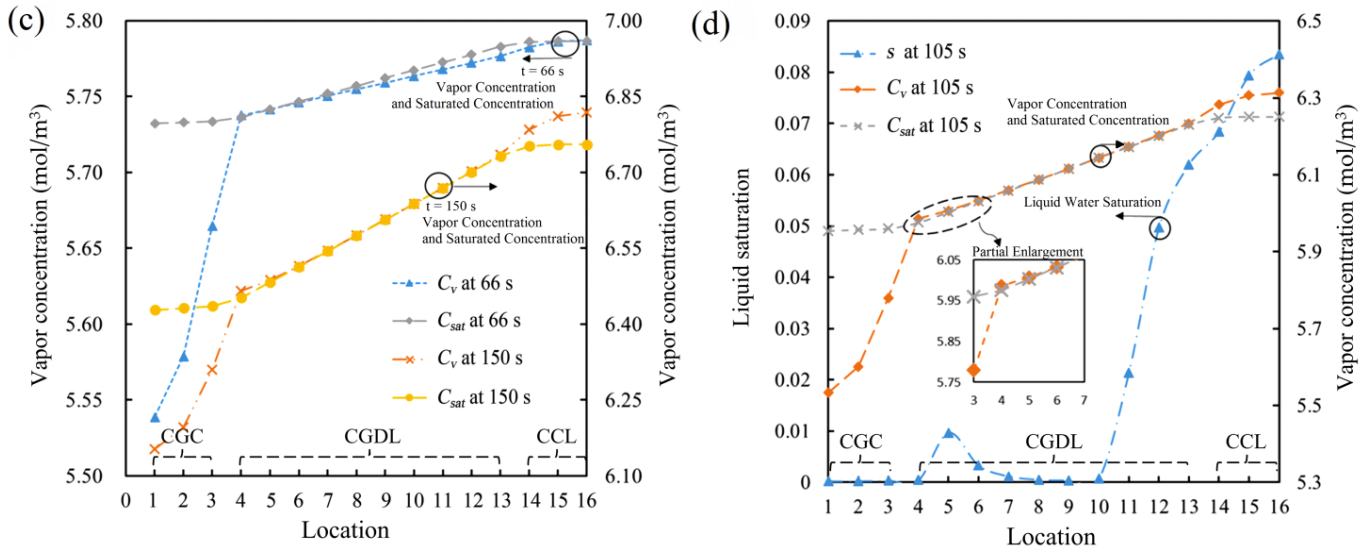

Figure 8. Water vapor and liquid water characteristics in the cathode: (**a**) changes in water vapor concentration, (**b**) changes in liquid water saturation, (**c**) comparison of water vapor concentration and its saturated value at 66 s and 150 s, and (**d**) relationship of liquid water saturation and water vapor concentration at 105 s.

The variations in the liquid water saturation are shown in Figure 8b. Liquid water started to generate at 66 s, and its saturation value increased with the increase in current density. At the beginning of liquid water generation in the CCL, the liquid saturation first reached a high value and then decreased. This phenomenon can be explained by Equations (12) and (13), which describe the relationship between the diffusivity of liquid water and the liquid saturation. The diffusion coefficient at the beginning was 0, and it increased with the liquid saturation, indicating that the liquid water transfer rate was positively correlated with the liquid saturation. When the amount of liquid water transferred to the CGDL is higher than that generated in the CCL, the liquid saturation decreased until a steady state was established. The CGDL began to fill with liquid water at 150 s, and after that, the liquid water saturation in each region became stable. The distributions of the vapor concentrations and saturated concentrations at 66 s and 150 s are plotted in Figure 8c. The vapor concentration in the CL reached its saturated value at 66 s, and after that, excessive water vapor started to condense. At 150 s, the vapor concentrations in all areas of the GDL and CL reached their saturated values. There was a concentration gradient in the gas channels due to the purging by the inlet unsaturated gas. The vapor concentrations in these regions were lower than their saturated values, which caused liquid water in the first region of GDL to be removed by the unsaturated gas.

Except for the conditions under which PEM was fully hydrated, the vapor concentration close to the CL was higher than that close to the gas channel, and liquid water in the second region of the GDL formed earlier than that in the fifth region, as circled in Figure 8b. This phenomenon can be explained by the relationship between the vapor concentrations and liquid saturation at 105 s shown in Figure 8d, in which the vapor concentration in the second region was slightly higher than its saturated value, resulting in liquid water formation. There are two main reasons for the liquid water generation: one is that the temperature decreased from the CCL to CEP, causing the saturated vapor concentration to decrease accordingly; the other is that the inlet gas was so wet that its relative humidity reached 80%, resulting in a high vapor concentration in the region close to the gas channel.

5.3. Distributions of Water Vapor and Liquid Water in the Anode Side

The distributions of and variations in vapor and liquid in the anode side during operation are shown in Figure 9. As shown in Figure 9a, the vapor concentration increased

continuously within the first 500 s as the density increased from 0.1 to 1.2 A/cm^2, while it decreased after 500 s, similar to the cathode, as shown in Figure 8a. The changes in liquid saturation in the anode were complicated. As shown in Figure 9b, liquid water was generated in the ACL and the first region of the GDL at almost the same time, and it flowed to the other regions later. Liquid water appeared latest in the fifth region of the GDL. The current density varied from 0.1 to 0.8 A/cm^2 within 70 to 300 s, and the liquid saturation in each region of the anode increased accordingly. After that, liquid saturation in the AGDL and ACL decreased, even if the current density continued to increase, which was quite different from the variations at the cathode. As described in Section 5.1, the temperature increased with the current density, and evaporation occurred when the increase in the saturated vapor concentration exceeded that of the vapor concentration. More liquid water was generated after 500 s because the current density decreased from 1.2 to 0.8 A/cm^2 and the temperature decreased accordingly.

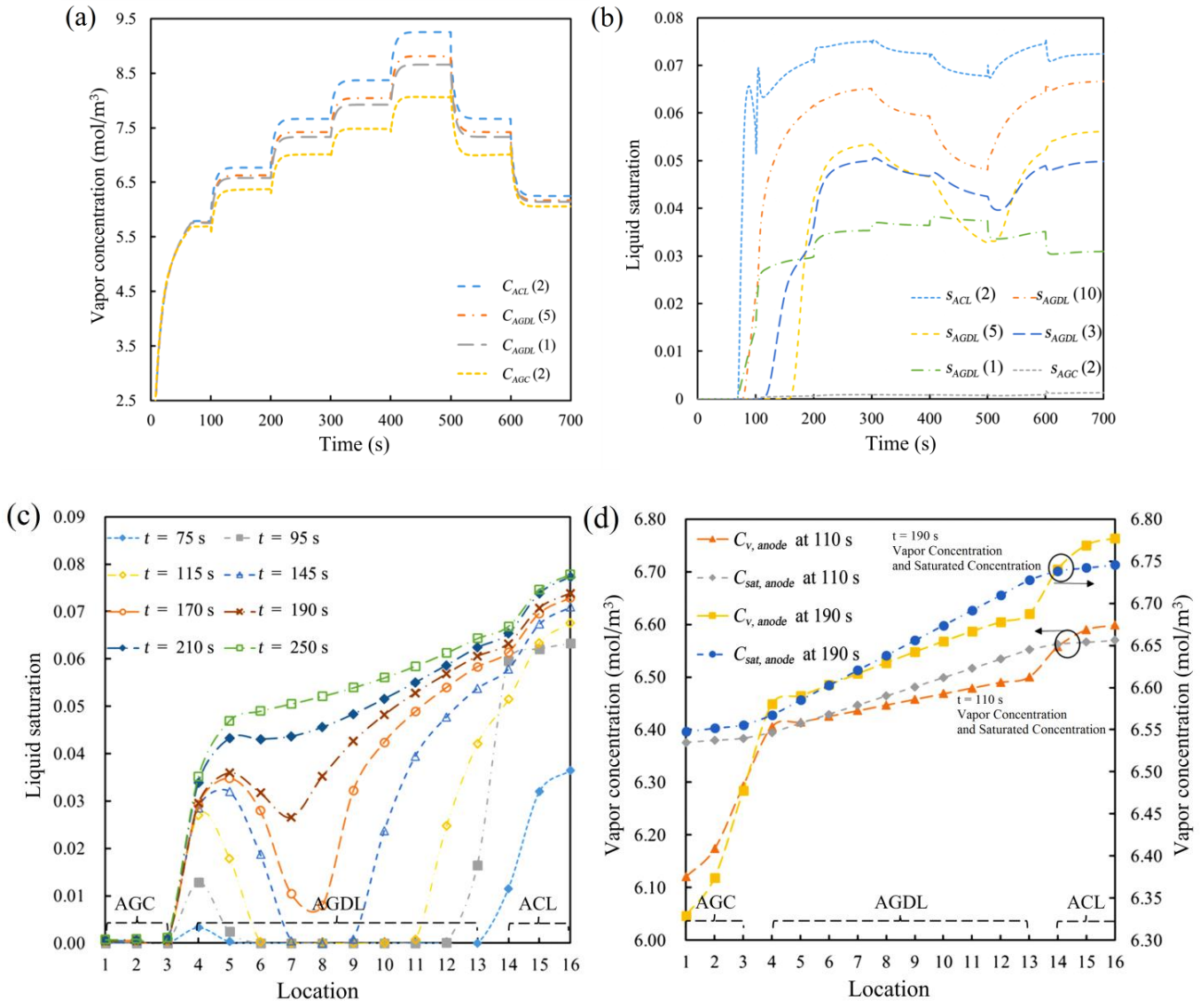

Figure 9. Water vapor and liquid water characteristics in the anode: (**a**) changes in the water vapor concentration, (**b**) changes in the liquid water saturation, (**c**) distributions of liquid saturation from 75 s to 250 s, and (**d**) relationship between the water vapor concentrations and their saturated values at 110 s and 190 s.

The distributions of liquid water from 75 to 250 s are exhibited in Figure 9c. It can be seen that liquid water first formed in the ACL and the first region of the AGDL at almost the same time, while it appeared latest in the middle of the AGDL. the liquid saturation in the AGDL and ACL increased continuously during the operation of the PEMFC, and a gradient of liquid saturation from the ACL to AGC was formed in the end. The relationships between the vapor concentration and the saturated vapor concentration at 110 and 190 s are plotted in Figure 9d. Only the vapor concentration in the ACL and regions close to the gas channel was higher than the saturated values. At the same time, evaporation occurred in the unsaturated areas, i.e., the middle of the GDL. When more liquid water flowed into the unsaturated regions than the amount of evaporated water, it accumulated in these areas. The liquid saturation in the first region of the GDL at the anode was higher than that at the cathode. The reason was that gas velocity in the AGC was lower than that in the CGC; hence, the anode gas had a weaker ability to remove water from the cells.

5.4. Distributions of Dissolved Water

It was assumed that water was initially generated in the ionomers of the CCL, which could either transfer to the anode across the membrane or transform between dissolved water and water vapor. The variations in the water contents in the CCL, PEM, and ACL are shown in Figure 10a. The water content increased quickly in the first 90 s and reached a steady state. After 100 s, the water contents in the three layers remained stable and swung slightly as the current density varied. The swing was due to sudden changes in CCL water generation. When the current density jumped to a higher level, more water was generated immediately. At this point, the dissolved water was unable to diffuse in time, leading to temporary increases or decreases in the water content. During the initial working process, the relationship between the water content in the second region of the CCL (blue line) and its equilibrium value (orange line) is shown in Figure 10b. As the initial value of the water content was 4, and the inlet gases at both sides always had high relative humidity, the membrane was fully humidified by the inlet gases. In the first 30 s, the water content was lower than the equilibrium value, indicating that vapor would transform into dissolved water. After 30 s, the water content was higher than its equilibrium value and the dissolved water started to evaporate into vapor in the CCL.

The distributions of the water content from the CCL to the ACL at 150 s, 250 s, 350 s, and 450 s are plotted in Figure 10c. Owing to water generation in the CCL, a water content gradient from the CCL to the ACL formed. In the CCL, the water content decreased slightly when the current density increased from 0.8 A/cm^2 at 250 s to 1.2 A/cm^2 at 450 s. In the ACL, the water content continued to decrease when the current density increased from 0.5 A/cm^2 at 150 s to 1.2 A/cm^2 at 450 s. According to Equations (18)–(20), the equilibrium water content was relevant to the liquid water saturation in the CL and the temperature of ionomers. The low liquid saturation and high temperature caused the water content to decrease. Although the current density increased from 0.5 to 1.2 A/cm^2, generating more liquid water, the temperature also increased.

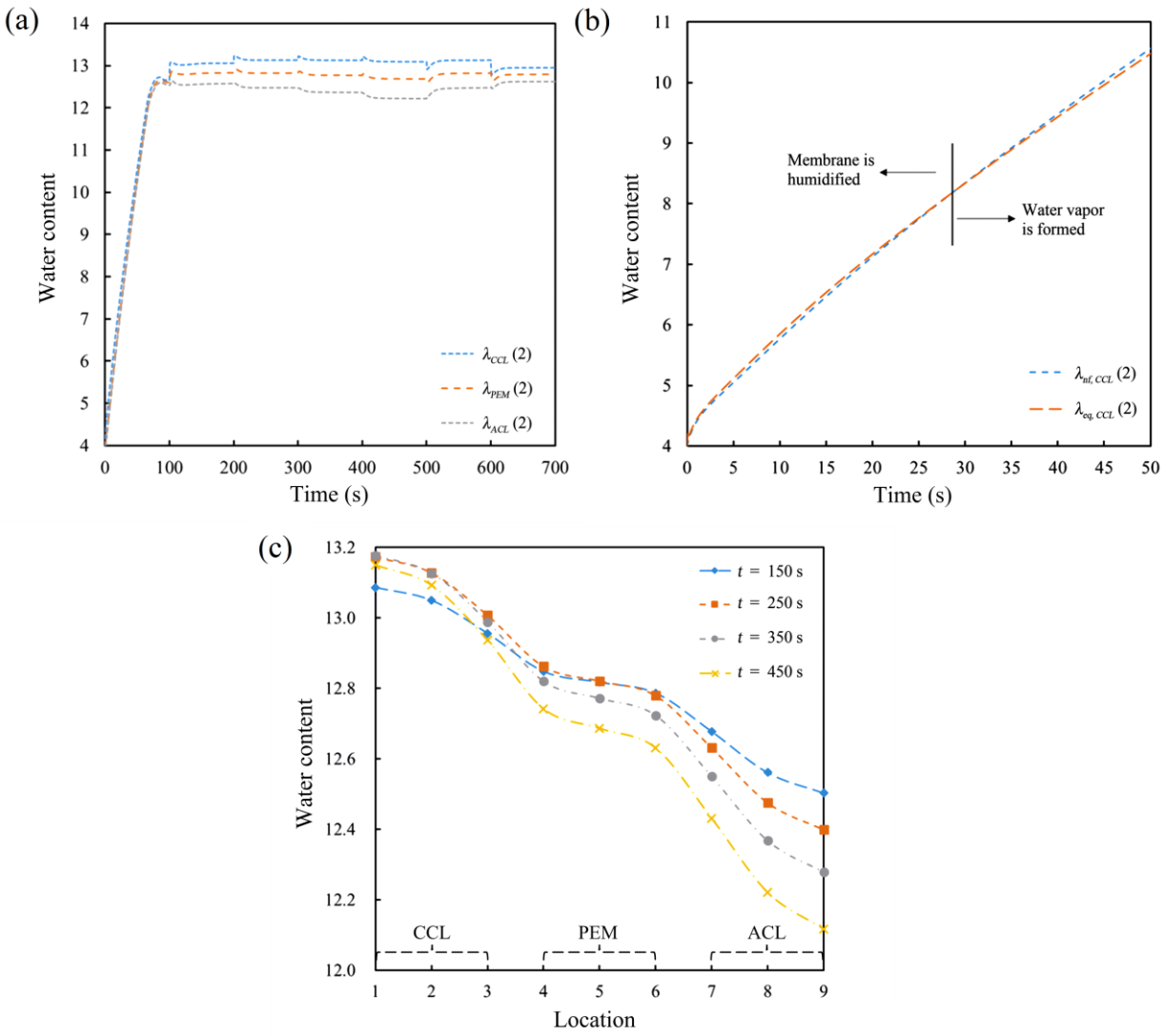

Figure 10. Dissolved water characteristics: (**a**) changes in the water content in the ACL, PEM, and CCL, (**b**) comparison of the dissolved water content and its equilibrium value in the second region of the ACL from 0 s to 50 s, and (**c**) distributions of the water content from the CCL to ACL at 150 s, 250 s, 350 s, and 450 s.

6. Conclusions

In this work, a one-dimensional transient non-isothermal model was built using MATLAB R2019a to investigate the effects of heat transport on two-phase flow in a PEMFC. The cell was discretized into 39 control volumes to study the characteristics of the gas concentration, liquid water saturation, and temperature in the cell. The variations in the heat and water distributions in the cell were analyzed under a loading–unloading operation. The following conclusions can be drawn:

(1) In a PEMFC stack, heat is mainly generated in the CCL, PEM, and ACL, and dissipated near cooling channels and endplates. Thus, the heat continuously transfers from the CCL to both the cathode and anode endplates. The water phase change between liquid and vapor strongly depends on the saturation vapor pressure. Liquid water is generally generated in the CCL first. When the gas relative humidity at the entrance of the gas channels is too high and the temperature difference in a cell is too large, the partial pressure of water vapor in the GDL close to the gas channels will be higher than the saturation vapor pressure, which will also lead to liquid water generation;

(2) The best condition for the water content in a PEMFC is when the water in the CL is just saturated. At this time, the mass transfer loss is the lowest and the ohmic loss is relatively low, leading to the highest output voltage. It is necessary to balance the water production and drainage to make the water just saturated. If the water is discharged as vapor, water drainage is dependent on the relative humidity and flow rate of the inlet gases, while the production depends on the current density. As a result, the optimal operating temperature increases with the increase in current density;
(3) Under a low current density, increasing the relative humidity of inlet gases contributes to a rapid hydrating process in PEMs, reducing the ohmic loss and increasing the output voltage. As the current density increases, the demand for the relative humidity of inlet gases gradually decreases due to the increase in water production. However, an excessively high inlet relative humidity leads to water accumulation in the cell and impedes gas transfer under a high current density, which will eventually cause flooding;
(4) The reaction gas at the cathode is air with a high mass flow rate compared with hydrogen at the anode. Although water is mainly generated in the CCL, a large air flux in the gas channels can effectively blow the liquid water out of the CCL and CGDL to avoid flooding in the cathode side. However, due to the low inlet gas flow rate at the anode, the accumulated liquid water cannot be purged in time under conditions with a high inlet relative humidity or high current density. The liquid water may block the anode gas channels, GDL, and CL, causing anode flooding.

Author Contributions: Conceptualization, D.G. and S.X.; methodology, Y.G.; software, D.G.; validation, X.W.; formal analysis, X.W.; investigation, Y.G.; resources, S.X.; data curation, D.G.; writing—original draft preparation, D.G.; writing—review and editing, Y.G.; visualization, Y.G.; supervision, S.X.; project administration, D.G.; funding acquisition, S.X. All authors have read and agreed to the published version of the manuscript.

Funding: This research was supported by the National Natural Science Foundation of China (Grant No.22279091) and the National Key R&D Program of China (Grant No. 2017YFB0102802).

Data Availability Statement: Not applicable.

Conflicts of Interest: The authors declare no conflict of interest.

Nomenclature

a	Water activity
A	Area (m^2)
C	Molar concentration (mol m^{-3})
C_p	Specific heat (J kg^{-1} K^{-1})
d	Diameter (m)
D	Mass diffusivity (m^2 s^{-1})
E	Potential (V)
EW	Equivalent weight of membrane (kg mol^{-1})
F	Faraday's constant (C mol^{-1})
h	Latent heat (J kg^{-1})
i	Current density (A m^{-2})
j	Volumetric transfer current (A m^{-3})
k	Thermal conductivity (W m^{-1} K^{-1})
K	Permeability (m^2)
L	Length (m)
M	Molecular weight (kg mol^{-1})
N	Molar flow rate (mol s^{-1})
P	Pressure (Pa)
Q	Heat source
R	Gas constant (J mol^{-1} K^{-1}), resistance (Ω)

RH	Relative humidity
s	Liquid saturation
S	Source terms, entropy (J mol^{-1} K^{-1})
t	Time (s)
T	Temperature (K)
u	Velocity (m s^{-1})
U	Voltage (V)
V	Volume flow rate (m^3 s^{-1})
x	Molar fraction
X	Liquid to gas velocity ratio
Z	Number of gas channels
Greek	
α	Transfer coefficient
ε	Porosity
γ	Water phase change rate (s^{-1})
μ	Dynamic viscosity (kg m^{-1} s^{-1})
σ	Surface tension (N m^{-1})
θ	Contact angle ($^\circ$)
ρ	Density (kg m^{-3})
ω	Volume fraction of ionomer
λ	Water content in ionomer
ξ	Phase change rate (s^{-1})
η	Over potential (V)
δ	Thickness (m)
κ	Ionic conductivity (S m^{-1})
ψ	Stoichiometry ratio
Subscripts and superscripts	
act	Activation
an	Anode
c	Carbon
ca	Cathode
ch	Channel
con	Condensation
$cool$	Coolant
di	Dissolved
dmw	Dissolved membrane water
dv	Dissolved water to vapor (vice versa)
eff	Effective
ele	Electron
eq	Equilibrium
end	End-plate
env	Environment
eva	Evaporation
g	Gas
H^2	Hydrogen
i	Gas species
in	Inlet
ion	Ionomer
lq	Liquid
mem	Membrane
mt	Mass transfer
nu	Knudsen
$nerst$	Nernst
oh	Ohmic
out	Outlet

O^2	Oxygen
r	Relative
ref	Reference
sat	Saturation
w	Water
v	Vapor
Abbreviations	
CL	Catalyst layer
GDL	Gas diffusion layer
AEP	Anode end-plate
ACG	Anode coolant channel
AGC	Anode gas channel
AGDL	Anode gas diffusion layer
ACL	Anode catalyst layer
CEP	Cathode end-plate
CCC	Cathode coolant channel
CGC	Cathode gas channel
CGDL	Cathode gas diffusion layer
CCL	Cathode catalyst layer
EOD	Electro-osmotic drag
PEM	Polymer electrolyte membrane
PEMFC	Polymer electrolyte membrane fuel cell

References

1. El-Mossalamy, E.H.; Batouti, M.E.L.; Fetouh, H.A. The role of natural biological macromolecules: Deoxyribonucleic and ribonucleic acids in the formulation of new stable charge transfer complexes of thiophene Schiff bases for various life applications. *Int. J. Biol. Macromol.* **2021**, *193*, 1572–1586. [CrossRef] [PubMed]
2. Sallam, E.R.; Khairy, H.M.; Elshobary, M.; Fetouh, H.A. Application of Algae for Hydrogen Generation and Utilization. In *Handbook of Research on Algae as a Sustainable Solution for Food, Energy, and the Environment*; IGI Global: Hershey, PA, USA, 2022; pp. 354–378.
3. O'hayre, R.; Cha, S.-W.; Colella, W.; Prinz, F.B. *Fuel Cell Fundamentals*; John Wiley & Sons: Hoboken, NJ, USA, 2016.
4. Yang, X.G.; Ye, Q.; Cheng, P. Matching of water and temperature fields in proton exchange membrane fuel cells with non-uniform distributions. *Int. J. Hydrogen Energy* **2011**, *36*, 12524–12537. [CrossRef]
5. Jiao, K.; Li, X.G. Water transport in polymer electrolyte membrane fuel cells. *Prog. Energy Combust. Sci.* **2011**, *37*, 221–291. [CrossRef]
6. Bazylak, A. Liquid water visualization in PEM fuel cells: A review. *Int. J. Hydrogen Energy* **2009**, *34*, 3845–3857. [CrossRef]
7. Ous, T.; Arcoumanis, C. Degradation aspects of water formation and transport in Proton Exchange Membrane Fuel Cell: A review. *J. Power Sources* **2013**, *240*, 558–582. [CrossRef]
8. Schmittinger, W.; Vahidi, A. A review of the main parameters influencing long-term performance and durability of PEM fuel cells. *J. Power Sources* **2008**, *180*, 1–14. [CrossRef]
9. Hasegawa, T.; Imanishi, H.; Nada, M.; Ikogi, Y. *Development of the Fuel Cell System in the Mirai FCV*; SAE Technical Paper: Detroit, MI, USA, 2016. [CrossRef]
10. Xing, L.; Du, S.F.; Chen, R.; Mamlouk, M.; Scott, K. Anode partial flooding modelling of proton exchange membrane fuel cells: Model development and validation. *Energy* **2016**, *96*, 80–95. [CrossRef]
11. O'Rourke, J.; Ramani, M.; Arcak, M. In situ detection of anode flooding of a PEM fuel cell. *Int. J. Hydrogen Energy* **2009**, *34*, 6765–6770. [CrossRef]
12. Anderson, R.; Blanco, M.; Bi, X.T.; Wilkinson, D.P. Anode water removal and cathode gas diffusion layer flooding in a proton exchange membrane fuel cell. *Int. J. Hydrogen Energy* **2012**, *37*, 16093–16103. [CrossRef]
13. Jiao, K.; Li, X.G. Three-dimensional multiphase modeling of cold start processes in polymer electrolyte membrane fuel cells. *Electrochim. Acta* **2009**, *54*, 6876–6891. [CrossRef]
14. Xu, P.; Xu, S.C. Three-dimensional Modeling of Gas Purge in a Polymer Electrolyte Membrane Fuel Cell with Co-flow and Counter-flow Pattern. *Fuel Cells* **2017**, *17*, 794–808. [CrossRef]
15. Amamou, A.; Kandidayeni, M.; Boulon, L.; Kelouwani, S. Real time adaptive efficient cold start strategy for proton exchange membrane fuel cells. *Appl. Energy* **2018**, *216*, 21–30. [CrossRef]
16. Wang, Y. Porous-Media Flow Fields for Polymer Electrolyte Fuel Cells II. Analysis of Channel Two-Phase Flow. *J. Electrochem. Soc.* **2009**, *156*, B1134–B1141. [CrossRef]
17. Park, H. Effect of the hydrophilic and hydrophobic characteristics of the gas diffusion medium on polymer electrolyte fuel cell performance under non-humidification condition. *Energy Convers. Manag.* **2014**, *81*, 220–230. [CrossRef]

18. Chun, J.H.; Park, K.T.; Jo, D.H.; Kim, S.G.; Kim, S.H. Numerical modeling and experimental study of the influence of GDL properties on performance in a PEMFC. *Int. J. Hydrogen Energy* **2011**, *36*, 1837–1845. [CrossRef]
19. LaManna, J.M.; Kandlikar, S.G. Determination of effective water vapor diffusion coefficient in pemfc gas diffusion layers. *Int. J. Hydrogen Energy* **2011**, *36*, 5021–5029. [CrossRef]
20. Pasaogullari, U.; Wang, C.Y. Two-phase transport and the role of micro-porous layer in polymer electrolyte fuel cells. *Electrochim. Acta* **2004**, *49*, 4359–4369. [CrossRef]
21. Ma, L.A.; Liu, Z.S.; Huang, C.; Chen, S.H.; Meng, G.W. Microstructure changes induced by capillary condensation in catalyst layers of PEM fuel cells. *Int. J. Hydrogen Energy* **2010**, *35*, 12182–12190. [CrossRef]
22. Ju, H.; Meng, H.; Wang, C.Y. A single-phase, non-isothermal model for PEM fuel cells. *Int. J. Heat Mass Transf.* **2005**, *48*, 1303–1315. [CrossRef]
23. Wang, Y.; Basu, S.; Wang, C.Y. Modeling two-phase flow in PEM fuel cell channels. *J. Power Sources* **2008**, *179*, 603–617. [CrossRef]
24. Um, S.; Wang, C.Y. Computational study of water transport in proton exchange membrane fuel cells. *J. Power Sources* **2006**, *156*, 211–223. [CrossRef]
25. Xing, L.; Liu, X.T.; Alaje, T.; Kumar, R.; Mamlouk, M.; Scott, K. A two-phase flow and non-isothermal agglomerate model for a proton exchange membrane (PEM) fuel cell. *Energy* **2014**, *73*, 618–634. [CrossRef]
26. Haddad, D.; Benmoussa, H.; Bourmada, N.; Oulmi, K.; Mahmah, B.; Belhamel, M. One dimensional transient numerical study of the mass heat and charge transfer in a proton exchange membrane for PEMFC. *Int. J. Hydrogen Energy* **2009**, *34*, 5010–5014. [CrossRef]
27. Hu, J.M.; Li, J.Q.; Xu, L.F.; Huang, F.S.; Ouyang, M.G. Analytical calculation and evaluation of water transport through a proton exchange membrane fuel cell based on a one-dimensional model. *Energy* **2016**, *111*, 869–883. [CrossRef]
28. Sallam, E.R.; Khairy, H.M.; Elnouby, M.S.; Fetouh, H.A. Sustainable electricity production from seawater using Spirulina platensis microbial fuel cell catalyzed by silver nanoparticles-activated carbon composite prepared by a new modified photolysis method. *Biomass Bioenergy* **2021**, *148*, 106038. [CrossRef]
29. Sallam, E.R.; Fetouh, H.A. Comparative Study for the Production of Sustainable Electricity from Marine Sediment Using Recyclable Low-Cost Solid Wastes Aluminum Foil and Graphite Anodes. *Chemistryselect* **2022**, *7*, e202103972. [CrossRef]
30. Nam, J.H.; Lee, K.J.; Hwang, G.S.; Kim, C.J.; Kaviany, M. Microporous layer for water morphology control in PEMFC. *Int. J. Heat Mass Transf.* **2009**, *52*, 2779–2791. [CrossRef]
31. Wang, Y.; Chen, K.S. *PEM Fuel Cells: Thermal and Water Management Fundamentals*; Momentum Press: New York, NY, USA, 2013.
32. Motupally, S.; Becker, A.J.; Weidner, J.W. Diffusion of water in Nafion 115 membranes. *J. Electrochem. Soc.* **2000**, *147*, 3171–3177. [CrossRef]
33. Zawodzinski, T.A.; Springer, T.E.; Uribe, F.; Gottesfeld, S. Characterization of Polymer Electrolytes for Fuel-Cell Applications. *Solid State Ionics* **1993**, *60*, 199–211. [CrossRef]
34. Springer, T.E.; Zawodzinski, T.A.; Gottesfeld, S. Polymer Electrolyte Fuel-Cell Model. *J. Electrochem. Soc.* **1991**, *138*, 2334–2342. [CrossRef]
35. Fox, R.W.; McDonald, A.T.; Pritchard, P.J. *Introduction to Fluid Mechanics*; John Wiley & Sons, Inc.: New York, NY, USA, 1994.
36. Chen, Y.S.; Peng, H. A segmented model for studying water transport in a PEMFC. *J. Power Sources* **2008**, *185*, 1179–1192. [CrossRef]
37. Li, R.X. *Finite Volume Method Fundamentals*; National Defense Industry: Arlington, VA, USA, 2008.
38. El Batouti, M.; Sadik, W.; Eldemerdash, A.G.; Hanafy, E.; Fetouh, H.A. New and innovative microwave-assisted technology for synthesis of guar gum-grafted acrylamide hydrogel superabsorbent for the removal of acid red 8 dye from industrial wastewater. *Polym. Bull.* **2022**, 1–25. [CrossRef]
39. Um, S.; Wang, C.Y. Three-dimensional analysis of transport and electrochemical reactions in polymer electrolyte fuel cells. *J. Power Sources* **2004**, *125*, 40–51. [CrossRef]
40. Yang, X.G.; Zhang, F.Y.; Lubawy, A.L.; Wang, C.Y. Visualization of liquid water transport in a PEFC. *Electrochem. Solid-State Lett.* **2004**, *7*, A408–A411. [CrossRef]